

1           **AIR-SEA INTERACTIONS FROM WESTERLY WIND BURSTS DURING**  
2           **THE NOVEMBER 2011 MJO IN THE INDIAN OCEAN**

3

4     James N. Moum, Simon P. de Szoek, William D. Smyth, James B. Edson, H. Langley  
5     DeWitt, Aurélie J. Moulin, Elizabeth J. Thompson, Christopher J. Zappa, Steven A.  
6     Rutledge, Richard H. Johnson and Christopher W. Fairall

7

8     **AFFILIATIONS:** MOUM, DESZOEKE, SMYTH, MOULIN – College of Earth, Ocean and Atmospheric  
9     Sciences, Oregon State University, Corvallis , OR; EDSON – Department of Marine Sciences, University of  
10    Connecticut, Groton, CT; DEWITT – NOAA Pacific Marine Environmental Laboratory, Seattle, WA;  
11    THOMPSON, RUTLEDGE, JOHNSON – Department of Atmospheric Sciences, Colorado State University, Fort  
12    Collins, CO; ZAPPA - Ocean and Climate Physics Division, Lamont-Doherty Earth Observatory of  
13    Columbia University, Palisades, NY; FAIRALL – NOAA Earth System Research Laboratory, Boulder, CO

14

15    **CORRESPONDING AUTHOR:** James N. Moum, College of Earth, Ocean and Atmospheric Sciences,  
16    Oregon State University, Corvallis, OR 97331-5503  
17    e-mail: [moum@coas.oregonstate.edu](mailto:moum@coas.oregonstate.edu)

18

19    *Capsule*

20    Detailed observations from 1 km beneath to 20 km above, and increasing density toward  
21    the sea surface, reveal the complex interactions in Indian Ocean westerly wind bursts  
22    associated with the Madden-Julian Oscillation.

23

24 *Abstract*

25 The complete life cycles of three Madden-Julian Oscillation (MJO) events were observed  
26 over the Indian Ocean by the DYNAMO (Dynamics of the MJO) experiment. During  
27 November 2011, we observed intense multiscale interactions *within* an MJO convective  
28 envelope, including exchanges between synoptic, meso-, convective- and turbulence  
29 scales in both atmosphere and ocean, complicated by a developing tropical cyclone near  
30 0°N, 80°E, the site of the Research Vessel *Roger Revelle*. Embedded within the MJO  
31 event, two bursts of sustained westerly wind ( $>10 \text{ m s}^{-1}$ , 0–8 km height) and enhanced  
32 precipitation passed over the ship, each propagating eastward at roughly the  
33 convectively-coupled Kelvin wave speed ( $\sim 8.6 \text{ m s}^{-1}$ ). The ocean response was rapid,  
34 energetic, and complex, accelerating the Yoshida-Wyrtki Jet at the equator from less than  
35  $0.5 \text{ m s}^{-1}$  to more than  $1.5 \text{ m s}^{-1}$  in 2 days. This doubled the eastward transport along the  
36 ocean’s equatorial waveguide. Subsurface turbulent heat fluxes were comparable to the  
37 net surface heat flux, thus playing a comparable role in cooling the sea surface. The  
38 sustained eastward surface jet continued to energize shear-driven entrainment at its base  
39 after the MJO wind bursts subsided, thereby further modifying sea surface temperature  
40 for a period of several weeks thereafter.

41

42

43     *Introduction*

44     The Madden-Julian Oscillation (MJO; Madden and Julian, 1971, 1972) is a disturbance  
45     of the atmosphere over tropical oceans associated with surface westerly wind bursts, deep  
46     convection and heavy precipitation. It originates in the Indian Ocean and travels at  
47     roughly  $5 \text{ m s}^{-1}$  across the ocean basin, sometimes circumnavigating the globe at the  
48     equator with a period between 30-90 days (Zhang 2005). This phenomenon is a  
49     fundamental contribution to Earth's weather and climate systems globally on  
50     intraseasonal time scales (Zhang 2013). Yet, MJO prediction is unsatisfactory, in large  
51     part due to insufficient representations of the multiscale processes involved in the model,  
52     which come from a lack of adequate measurement and a thorough understanding of these  
53     processes. The contribution of atmosphere – ocean feedbacks to the emergence and  
54     evolution of the MJO remains unknown. This notion prompted DYNAMO's (Dynamics  
55     of the Madden-Julian Oscillation; <http://www.eol.ucar.edu/projects/dynamo/>) hypothesis  
56     III:

57         *The barrier layer, wind- and shear-driven mixing, shallow thermocline, and*  
58         *mixing-layer entrainment all play essential roles in MJO initiation in the Indian*  
59         *Ocean by controlling the upper-ocean heat content and SST, and thereby surface*  
60         *flux feedback.*

61     As part of the DYNAMO experiment in boreal fall 2011 through early 2012 (Yoneyama  
62     et al., 2013), a particularly well-instrumented measurement program was conducted at the  
63     equator and  $80.5^\circ \text{ E}$  from the Research Vessel *Roger Revelle* (Figure 1) to make detailed  
64     observations of physical processes from 1 km below to 25 km above the sea surface. For  
65     as-yet unknown reasons, the passage/occurrence of MJO convective envelopes observed

66 at *Revelle* and elsewhere along the equator do not appear on a regular schedule (Zhang,  
67 2005). Between mid-October and mid-December, three MJOs were tracked across the  
68 Indian Ocean (Gottschalk et al. 2013; Yoneyama et al., 2013) and are identified as  
69 MJO1-3. MJO2 was the strongest of the three. On 24 November 2011, MJO2 crossed the  
70 position of the *Revelle*. At the same time, a low-level cyclonic rotation to the immediate  
71 north, between the horn of India and *Revelle*, intensified. This region was identified by  
72 the U.S. Joint Tropical Warning Center (JTWC) as a tropical disturbance and upgraded to  
73 a tropical cyclone on 26 November. This event was forecast with a lead time of 6 days  
74 and was not unexpected; nevertheless it caused significant loss of life and property  
75 damage along Sri Lanka's southeast coast (Sidebar 1).

76

### 77 *Measurements*

78 Instrumentation was installed on *Revelle* (Figure 1, Table 1) to obtain:

- 79 • atmospheric soundings (8/day) of velocity, temperature, relative humidity and  
80 pressure altitude;
- 81 • complete atmospheric surface turbulent flux measurements for comparison to  
82 bulk formulae using standard meteorological observations;
- 83 • boundary layer velocity profiles measurements using W-band Doppler radar  
84 and high-resolution Doppler lidar;
- 85 • continuous C-band Doppler radar scans measuring radial velocity and radar  
86 reflectivity;
- 87 • particle distributions and chemical composition of aerosols;
- 88 • upper ocean current profiles from hull-mounted Doppler sonar;

- 89           • water column optical profiles to determine the penetrating solar radiation, a  
90                 key contributor to air-sea heat exchanges;
- 91           • sea surface (skin) temperature from infrared radiometers;
- 92           • near-surface ocean temperature and salinity profiles from ~0.05-7 m depth  
93                 from a towed surface thermistor (seasnake) and fixed subsurface array (CT-  
94                 chain);
- 95           • continuous profiling (150-200 casts/day) of upper ocean temperature, salinity,  
96                 microscale shear and subsurface turbulent fluxes of heat, salt and momentum.

97      Longer time scale context for these measurements was provided by the nearby equatorial  
98      RAMA (The Research Moored Array for African-Asian-Australian Monsoon Analysis  
99      and Prediction; McPhaden et al., 2009) buoy at 0°, 80.5°E, which was heavily-  
100     instrumented to provide measurements of basic surface meteorological fields and  
101     subsurface density and current structure.

102

103     *Surface properties of MJOs at 0°, 80.5°E*

104      The MJO is identified by large scale, eastward-propagating negative anomalies of  
105      outgoing longwave radiation (OLR) at the top of the atmosphere, a quantity directly  
106      related to the intensity of atmospheric convection. Several distinct features common  
107      among the three MJOs observed between October and December 2011 appear in Figure  
108      2. On the equator at 80.5°E, active phases of the three MJOs were associated with  
109      negative OLR anomalies that persisted for periods of 5-10 days and coincide with  
110      negative anomalies in surface pressure (Figure 2a), consistent with the findings of  
111      Madden and Julian (1972). Each MJO is associated with one or more westerly wind

112 bursts of varying magnitude (Figure 2b) followed quickly by an eastward acceleration of  
113 near-surface zonal currents (Figure 2c). Prior to the active phase of the MJOs, sea surface  
114 temperatures (SST) steadily increased (Figure 2d). Especially during the suppressed  
115 phase when skies were clear and wind speed was low, a significant daily near-surface  
116 warming of up to 3°C was present in the rapid-response ship-based measurements,  
117 although this is averaged out in the daily RAMA data shown to express continuity.  
118 Strong negative excursions in surface air temperature reflect the effect of precipitation  
119 downdrafts (Figure. 2e). With the arrival of deep convection (low OLR) at the onset of  
120 the active phase, solar radiation at the sea surface decreased while the wind bursts  
121 increased latent cooling flux (about 0.5 Wm<sup>-2</sup> more latent cooling for each Wm<sup>-2</sup> of solar  
122 flux reduction). Consequently, the net surface heat flux changed sign from heating to  
123 cooling the sea surface (Figure 2f). This, plus the mixing of cool water from below,  
124 contributed to cooling of the upper ocean during MJO events (see discussion related to  
125 Figure 7).

126

127 OLR and pressure anomalies were largest during MJO2, as were the strength of the wind  
128 bursts and the increased zonal current velocities in the direction of the wind.  
129 Furthermore, the net surface heat fluxes were most strongly negative (which indicates sea  
130 surface cooling) and the change in SST greatest during MJO2. Since *Revelle* was in an  
131 ideal observational position with all systems working to record the full extent of the  
132 atmospheric structure and oceanic response to MJO2, we will now examine this event  
133 with the wide array of measurements available.

134

135 *Atmospheric structure of the MJO2 wind bursts*

136 A longitude-time Hovmoller plot of OLR averaged  $\pm 0.5^\circ$  about the equator indicates an  
137 envelope of low OLR (Figure 3; values within the closed contour [black] are less than  
138  $200 \text{ W m}^{-2}$ ), marking MJO2 as an eastward-moving disturbance at roughly  $5 \text{ m s}^{-1}$   
139 (Figure 3) that passed over the *Revelle* between about 23-29 November (Yoneyama et al.,  
140 2013). The TRMM precipitation signal in Figure 3a (color shaded) identifies two  
141 convectively-coupled or moist Kelvin waves moving at  $8.6 \text{ m s}^{-1}$  within the slower-  
142 moving envelope of low OLR that identifies MJO2 (Gottschalck et al. 2013). In time  
143 series from *Revelle*, each Kelvin wave is associated with a precipitating event (Figure 3b)  
144 and simultaneous wind burst (Figure 3c). Figure 3 thus illustrates the distinctive double  
145 wind burst and precipitation structure of MJO2. We refer to the two precipitation/wind  
146 events of MJO2 as westerly wind burst 1 and westerly wind burst 2 (WWB1 on 24  
147 November and WWB2 on 28 November). Wind stress at the leading edge of WWB1  
148 exceeded  $0.7 \text{ N m}^{-2}$  (at 10-minute average), the largest values observed at  $0^\circ, 80.5^\circ\text{E}$   
149 during DYNAMO.

150

151 Most of the precipitation associated with MJO2 fell within the two Kelvin wave  
152 envelopes (Figure 3b). Areal averaged precipitated rain (100 km range) was 37 mm  
153 during the 24 h period beginning 24 November 09:00 (all times UTC), the largest daily  
154 rain rate observed on the equator by *Revelle* during DYNAMO.

155

156 C-band radar estimates of precipitation at *Revelle* show a series of rain events irregularly  
157 spaced about every 36 h, prior to the arrival of the WWBs. High radar reflectivity in these

158 events indicate stronger precipitation originating from convective updrafts (Figure 3b).  
159 Widespread stratiform precipitation (with moderate radar reflectivity) increased  
160 substantially following the leading edges of WWB1 and WWB2. During each wind burst  
161 convective and stratiform rainfall contributed about equally to the total rainfall whereas  
162 prior to the WWBs the rainfall was approximately 80% convective. The increased  
163 contribution of stratiform rainfall to total rainfall during the active phase of MJO2 is  
164 consistent with previous studies of tropical precipitation over the ocean (GATE; Bell and  
165 Suhasini, 1994 and TOGA COARE; Short et al., 1997), and implies a deep “top-heavy”  
166 profile of latent heating (Schumacher et al., 2004) in the WWBs embedded within the  
167 MJO envelope.

168

169 Atmospheric soundings from *Revelle* show potential temperature anomalies ( $\theta$ , Figure  
170 4a), specific humidity anomalies (Figure 4b) and zonal wind (Figure 4c) associated with  
171 the two WWBs in MJO2. WWB1 was accompanied by a surface pressure drop and mean  
172  $8 \text{ cm s}^{-1}$  upward velocity over the northern DYNAMO array, compared to WWB2 with  
173 mean upward vertical velocity of  $6 \text{ cm s}^{-1}$  (Figure 4a), consistent with precipitation in the  
174 WWBs (Johnson and Ciesielski 2013).

175

176 In the convectively-suppressed period before the arrival of the WWBs (11-23  
177 November), trade cumulus clouds and occasional cumulus congestus clouds kept the mid-  
178 troposphere near saturation to an altitude of 3-8 km (Figure 4b). The time evolution of the  
179 high-resolution soundings suggests large scale descent motions over the ship in addition  
180 to the effects of the diurnal heating cycle and lateral advection. Anomalies of potential

181 temperature can be seen to descend on the order of  $1 \text{ cm s}^{-1}$  from 6-14 km on 11-18  
182 November and 1-8 December. At these times the humidity in the upper troposphere was  
183 anomalously low, and the descent was considerably above the height reached by  
184 convective clouds, indicated roughly by the 70% relative humidity contour (thin line,  
185 Figure 4b). In the week before the active phase of MJO2, the low to mid- troposphere  
186 gradually moistened and the moisture occasionally reached deeper into the troposphere,  
187 e.g. on 18, 20, and 22 November, presumably associated with intense convective rain  
188 events observed by C-band radar in Figure 3b. Specific humidity (Figure 4b) in the mid-  
189 and upper troposphere increased significantly above their average just prior to the onset  
190 of WWB1 (24 November) and WWB2 (28 November) and subsequently decreased  
191 during and immediately after the wind bursts. Maximum specific humidity anomalies  
192 were observed between 2-5 km with large positive anomalies up to 9 km during each  
193 WWB.

194

195 Zonal wind anomalies associated with the two westerly wind bursts arrived at the surface  
196 first, then penetrated to 8 km within one day (Figure 4c). These two wind events were  
197 separated by a day of weak, slightly easterly winds, with slightly drier air and little to no  
198 precipitation as seen on 26 November in Figure 4b. This was presumably because off-  
199 equatorial dry air was advected into *Revelle*'s sampling domain, likely associated with  
200 the synoptic scale environment surrounding the tropical cyclone to the north. Easterlies in  
201 the upper troposphere (Figure 4c; 10-16 km) began at the onset of MJO2 and persisted  
202 for 2 weeks. While WWBs are commonly associated with MJO events, this particular  
203 separation of westerlies into two distinct bursts, and their vertical tilt during MJO2, bears

204 the signature of convectively-coupled Kelvin waves (Kiladis et al., 2009) propagating  
205 over the ship during MJO2 (Gottschalck et al. 2013). Such propagating disturbances are  
206 frequently associated with the active phase of the MJO, albeit with larger phase speeds  
207 than observed here (typically  $10\text{-}17 \text{ m s}^{-1}$ ; Roundy, 2008). The temperature and moisture  
208 structures of the two WWBs are consistent with that shown to exist in association with  
209 convectively coupled Kelvin waves observed over the Pacific Ocean and described by  
210 Straub and Kiladis (2002) and Kiladis et al. (2009). In both the Indian and Pacific basins,  
211 positive thermal and moisture anomalies have a westward tilt with height, as does the  
212 zonal wind anomaly. However, the phasing of the anomalies over the Indian Ocean  
213 differs slightly from that observed over the Pacific. In the lower troposphere the positive  
214 moisture and temperature anomalies during the DYNAMO WWBs precede the zonal  
215 wind anomalies by approximately one and two days, respectively, whereas in the Pacific  
216 the phase lag between the two is approximately two and three days, respectively. The  
217 positive potential temperature anomalies in the upper troposphere during the convectively  
218 active periods reflect the effects of latent heat release while the cool anomalies at low  
219 levels shortly thereafter indicate the cumulative effects of convective downdrafts. A day  
220 or two following the peak westerlies, drying is observed in the lower troposphere  
221 between 2 and 5 km (Figure 4b), coinciding with prevalent stratiform precipitation  
222 (Figure 3b). The evolution of the thermodynamic fields for both WWBs is consistent with  
223 the ship-borne radar findings showing a transition from a dominance of convective  
224 precipitation at the beginning to stratiform precipitation during each WWB (Figure 3).

225

226 Warming associated with the WWBs, Kelvin waves, and periods of prolonged stratiform  
227 rain, are the dominant mechanism for the potential temperature anomalies in Figure 4a. In  
228 the upper troposphere, two distinct positive potential temperature anomalies of about 3°  
229 C lead each of the WWBs by about one day. An explanation for this phase relationship  
230 could be that zonal convergence supplies the mass to rising updrafts, fueled by the latent  
231 heat of condensation and deposition. The vertical profile of latent heating for stratiform  
232 rain is “top-heavy” in the troposphere: heating at the top and cooling slightly in the  
233 boundary layer due to evaporating precipitation, consistent with  $\theta$  profiles in Figure 4a.  
234 This hypothesis also seems reconcilable with the observed specific humidity anomalies,  
235 which occur below the temperature anomalies suggesting that precipitation removes  
236 moisture from the upper troposphere through condensation.

237

238 We calculate the zonal convergence assuming it balances the divergence of vertical  
239 velocity in a two-dimensional form of mass conservation. Vertical velocities averaged  
240 over the entire 1000 km<sup>2</sup> domain during the precipitation events are on the order of 0.3-  
241 0.4 Pa s<sup>-1</sup> at 400 hPa. Assuming the phase speed of the convection is 9 m s<sup>-1</sup>, the wind in  
242 the lower troposphere would accelerate about 5 m s<sup>-1</sup> day<sup>-1</sup> in the rain event. The westerly  
243 winds are observed to accelerate at least twice this fast. The reason could be that the  
244 array-averaged vertical velocity underestimates the local equatorial vertical velocity in  
245 this event, or that there is significant meridional divergence neglected in this two-  
246 dimensional analysis. The warm anomalies last about 3 days each, and the potential  
247 temperature anomaly returns to nearly zero between the two warm anomalies. Potential  
248 temperature anomalies were small in the boundary layer and lower troposphere in the

249 week preceding the active phase of MJO2 (16-23November). Gradual warming of the  
250 upper troposphere ( $2^{\circ}\text{C}$ ) and diurnal warming ( $\sim 1^{\circ}\text{C}$  each day) above 6 km were more  
251 subtle than the two warm anomalies associated with the stratiform rain in the WWBs.  
252

253 Near-surface atmospheric cold pools occurred in both suppressed and active phases of the  
254 MJO, but were stronger and more frequent during the active phase than the suppressed  
255 phase (Figure 2e), with the largest air-surface temperature differences ( $>4^{\circ}\text{C}$ ) during  
256 WWB2 (Figure 4a,d). Mean values of sea-air temperature difference increased from  
257  $1.3^{\circ}\text{C}$  during the suppressed phases to  $2.1^{\circ}\text{C}$  during the active phases, indicating mean air  
258 temperature cooled more strongly than SST in active phases of the MJO. Gradual  
259 moistening of the near surface is observed prior to 24 November as seen in Figure 4e,  
260 mirroring the response of the lower to mid- troposphere. The specific humidity near the  
261 surface (Figure 4e) through the lower troposphere (Figure 4c) decreased during the  
262 WWBs. The SST and corresponding value of the sea surface specific humidity started to  
263 decrease as the daily averaged net heat flux changes sign around 21-22 November. This  
264 decrease is therefore associated with the onset of the isolated rain events rather than the  
265 widespread events characterized by deep convection and stratiform precipitation that  
266 began just prior to WWB1 on 24 November. Therefore, the onset of surface cooling is  
267 somewhat earlier than suggested by the conceptual model of Stephens et al. (2004). An  
268 investigation of whether the timing of events in MJO2 is representative of the other MJO  
269 events is ongoing. The physical processes responsible for the temperature response of the  
270 upper ocean are discussed in the following section.

271

272 *Ocean response to wind bursts during MJO2*

273 The leading edge of WWB1 arrived at *Revelle*'s site at 09:00 (all times UTC) on 24  
274 November, associated with the initial increase in wind stress from the preceding calm  
275 conditions (Figure 5a). The ensuing development of the surface wave field from the  
276 initial two-component swell (8, 13 s periods) prior to the arrival of WWB1 is seen in  
277 wave height measured from a Reigl laser altimeter on *Revelle*'s bow (Figure 5a-c).  
278 Directional wave spectra derived from ship's X-band radar via WaMoS processing  
279 (*Borge et al.*, 1999; *Cifuentes-Lorenzen et al.*, 2013; *Wyatt et al.*, 2003) identifies the 8 s  
280 swell direction as NNE and the 13 s swell from SSW. Wind stress began to slowly  
281 increase at about 08:00, to  $0.3 \text{ N m}^{-2}$  by 09:00, peaking at  $0.7 \text{ N m}^{-2}$  at 12:00 (30-minute  
282 averages shown on Figure 5). The peak in significant wave height lagged that of wind  
283 stress by 2 to 3 hours. The wave spectrogram shows the abrupt appearance of a  
284 narrowband wind wave field at 0.25-0.30 Hz (3-4s period) at 09:00, indicative of very  
285 young seas (low ratio of phase speed to wind speed,  $c_p / U_{10} = 0.5$ ). Thereafter, the  
286 spectrum of the wind waves broadened in frequency and increased in intensity, masking  
287 the original two-component swell by 12:00.

288

289 A more direct comparison of wave states before and after the arrival of WWB1 is seen in  
290 individual spectra (Figure 5c – here in variance-preserving form, where equal areas  
291 represent equal energies). These emphasize the amplification of the higher-frequency  
292 wind wave field and show the change in the lower-frequency swell components. The  
293 initial 13 s period waves lingered after the wind burst's arrival, but the 8 s swell  
294 diminished, replaced by a 9 s swell from due west, the direction of WWB1. The

295 contribution of the growing and breaking wind waves to marine aerosols in the lower  
296 atmosphere was significant (Sidebar 2).

297

298 The wind bursts' initial influence on the upper few meters of the ocean is seen in densely-  
299 sampled fast temperature sensors (FP07s) suspended from *Revelle*'s bow at 2.0, 3.9, and  
300 7.1 m (Figure 6). The net consequence of the MJO was to cool the sea surface (Figure  
301 2d), but the processes that modify SST were complex and cooling did not proceed  
302 uniformly in time. In particular, warming events noted in Figure 6 demonstrate non-  
303 uniform cooling. Prior to 08:00 on 24 November, net daytime surface heating created a  
304 warm layer in the upper several meters, the heating rate being modulated by variations in  
305 solar radiation. This temperature structure is representative of the thin diurnal warm layer  
306 of several K over the top meter or so that dominates the high frequency SST signal in  
307 Figure 2d. Optical profiles of penetrating solar radiation made from *Revelle* (Carter  
308 Ohlmann, UC Santa Barbara, pers. communication) suggest that 50% of solar heat was  
309 trapped in the upper 1.5 m. Solar heating above 2 m was even more intense than shown in  
310 Figure 6c,d. With the arrival of WWB1 on 24 November, the net surface heat flux  
311 changed sign and the daytime heating ended before 09:00 (Sunset is roughly 12:00 at  
312 *Revelle*'s location). An immediate result was the downward mixing of heat from the thin,  
313 diurnally-warmed layer at the surface to the sensors at 2.0, 3.9, and 7.1 m, which warmed  
314 during the first 15 minutes of the storm despite cooling from the atmosphere. Subsequent  
315 cooling of the upper 8 m was interrupted by a short heating event at 10:00, presumably  
316 associated with mixing of warm water from below, a consequence of the *barrier layer*  
317 (discussed further in reference to Figure 7).

318

319 Shortly after 10:00, temperature traces show a narrow band oscillation (periods 3-4  
320 minutes) of alternating cool and warm fluid. This suggests the presence of Langmuir  
321 circulations. These reach to the base of the mixed layer, entrain fluid from there, bringing  
322 it to the surface, all at a period consistent with Langmuir cell rotation. These signatures  
323 are consistent with high-frequency velocity signals measured by Doppler sonar.  
324 Langmuir circulations represent a unique sea surface cooling mechanism not directly  
325 included in our measurements of subsurface turbulent heat flux.

326

327 At greater depths, the development of temperature and salinity stratification shows how  
328 salinity contributes to MJO-related SST modification. This is revealed by time series of  
329 velocity, temperature, salinity and turbulence dissipation rate from the *Chameleon*  
330 turbulence profiler (Moum et al., 1995; Figure 7a-f). Before the arrival of WWB1, the  
331 upper 25 m of the water column was warm and fresh, so salinity dominated the  
332 stratification beneath the diurnal warm layer (at these salinities and temperatures, a 0.25  
333 psu change in salinity contributes an equivalent change in density as a 0.60°C change in  
334 temperature). This represents a classical example of *barrier layer* structure wherein the  
335 addition of saline stratification to thermal stratification complicates the ocean's response  
336 to surface forcing (Cronin and McPhaden, 1997). Barrier layers may contribute to  
337 intensification of tropical cyclones by partially insulating the sea surface against cooling  
338 from below caused by subsurface mixing (Balaguru et al., 2012). Details of the structure  
339 are shown with isotherm spacing in Figure 7h and isohaline spacing in Figure 7i  
340 contributing equally to density. It is evident that the halocline above 20 m depth

341 dominated the stratification in the first several hours of WWB1. The warm water at this  
342 depth was quickly mixed upward, contributing to the second warming event in Figure 6c.

343 At the same time, and despite heavy rainfall, sea surface salinity increased due to  
344 entrainment of salty water upward from the halocline. The halocline (and the mixed  
345 layer) deepened to the thermocline at 50 m depth a full 15 h after the arrival of WWB1.

346

347 A curious feature is the presence of biologically-generated turbulence during nighttime  
348 hours. This was associated with particularly energetic swimmers following the deep  
349 scattering layer comprised of zooplankton (which migrate down and out of the sunlit  
350 upper layers to avoid predators during the day) up into the euphotic zone to feed at night.

351 The signal is seen in the abrupt increase in turbulent dissipation at all depths above 60 m  
352 on the calm days (22, 23 November) preceding WWB1 (Figure 7f) and confirmed by  
353 comparison to acoustic volume backscatter estimates from high-frequency (120 kHz)  
354 acoustic measurements from a hull-mounted transducer. It has been observed that fish-  
355 aggregating devices (FADs) are particularly effective in the Indian Ocean (Moreno et al.  
356 2007) and it is likely that the ship acted as an FAD and that the observed biologically-  
357 generated turbulence was a local effect. The signature of the turbulence due to the forcing  
358 of WWB1 is much more intense, as evidenced by the deepening mixing which follows  
359 (and exceeds) the mixed layer depth in the first 24 h after the arrival of WWB1.

360

361 Steady equatorial easterlies in Pacific and Atlantic Oceans drive a westward surface  
362 current. Steady easterlies do not exist in the equatorial Indian Ocean, where reversing  
363 zonal winds cause intermittent amplification of an eastward-flowing surface current at the

364 equator, the Yoshida-Wyrtki Jet (Yoshida, 1959; Wyrtki, 1973) observed down to  $\sim$ 150  
365 m. For the first time, the details of the Indian Ocean jet spinup process were observed in  
366 the wake of MJO2. Before the arrival of WWB1, a weak eastward zonal surface current  
367 overlays a westward undercurrent (only the top of the undercurrent is seen in Figure 7c).  
368 In the first two days following the arrival of WWB1, the mixed layer cooled by almost  
369  $1^{\circ}\text{C}$  due to the combination of atmospheric cooling from above and mixing from below,  
370 roughly partitioned as 2/3 temperature change contribution from the atmosphere, 1/3  
371 from the ocean (based on turbulence heat flux estimates following Moum et al., 2009).  
372 The mixed layer deepened to 50 m after WWB1 and further after WWB2. The Yoshida-  
373 Wyrtki Jet accelerated (Figure 7 and Sidebar 3) to speeds in excess of  $1 \text{ m s}^{-1}$ , due almost  
374 solely to the excess of wind stress over turbulence friction at the base of the Jet.  
375 Subsequent, slow deceleration of the Jet following WWB2 was in reasonable balance  
376 with shear-generated turbulent friction at its base.

377

#### 378 *Summary*

379 The previous large-scale intensive tropical air-sea interaction experiment, the Tropical  
380 Ocean Global Atmosphere Coupled Ocean Atmosphere Response Experiment (TOGA-  
381 COARE, 1992-93) was designed to observe the evolution of the MJO as it propagated  
382 into the western equatorial Pacific warm pool. TOGA-COARE provided observations of  
383 an evolved state of the MJO with some of the same types of measurements deployed in  
384 DYNAMO without, however, the concentration of so many measurements on a single  
385 platform. Including new measurements described here (the development of the surface  
386 wave field and the injection of aerosols into the marine boundary layer), and some not, as

387 well as improved sampling (8 soundings per day in DYNAMO compared to 4 per day in  
388 TOGA-COARE), an unprecedented observational data set extending from 1 km beneath  
389 the sea surface to 20 km above, and with increasing concentration of measurements  
390 toward the sea surface, is in the process of being assembled and quality-controlled for  
391 future generations. Aside from their quality and density, these data represent the first  
392 detailed observations of the internal structure of convectively-coupled Kelvin waves  
393 embedded in an MJO, their influence on the ocean and the broad cross-equatorial  
394 structure, long-lasting effect and potential feedbacks caused by Yoshida-Wyrki Jets. We  
395 are excited by the prospects for contributing to significant improvements in  
396 understanding the MJO.

397

398 Our objective has been to present a description of the sequence of events in the  
399 atmosphere, upper ocean, and their interface prior to, during, and following active phases  
400 of the MJO from a particularly well-sampled location on the equator in the Indian Ocean.  
401 We note several general tendencies of the three MJOs observed in late 2011 as well as  
402 unique features of one MJO event in November 2011 (MJO2).

403

404 All three DYNAMO MJO events were characterized by low OLR that roughly matched  
405 the time scale of the low surface pressure signal at *Revelle*. During the suppressed phases,  
406 SST and oceanic heat storage rose day-by-day. SST exhibited a marked diurnal cycle  
407 under low winds, sunny skies, and inhibited atmospheric convection of limited area.  
408 MJO2 offers an illustrative example of the changes brought to the ocean-atmosphere  
409 system by the active phase. Two distinct westerly wind bursts/rain events formed within

410 MJO2, separated by 24 hour period of quiescent conditions. Warming of the deep  
411 troposphere was consistent with the shift in the precipitating cloud population; from  
412 convective precipitation of small area, to intense, deep convection briefly, and then  
413 widespread stratiform precipitation with weak, embedded convection. The stratiform rain  
414 pattern persisted for two days in each event, during which widespread cloudiness  
415 dramatically reduced the solar radiation reaching the surface. A deep (up to 8 km MSL)  
416 westerly wind anomaly developed following the heating in the upper troposphere.  
417 Westerly wind anomalies at the surface synchronous with the stratiform rain are  
418 consistent with zonal convergence supplying mass to updrafts fueled by latent heat of  
419 condensation. These weak convective updrafts feed the stratiform precipitation. It is not  
420 known at this time what role the large scale convergence by itself may have played in  
421 creating the stratiform precipitation. Each westerly wind burst significantly increased the  
422 surface wind stress, affecting the surface heat fluxes and turbulent mixing in the ocean.

423

424 SST rapidly decreased in response to surface fluxes and subsurface mixing. The decrease  
425 began during the earliest stage of the active phase (i.e., during isolated precipitating  
426 events), due to the ever-present latent and sensible heat exchange and reduction in solar  
427 insolation. These upward turbulent surface heat fluxes contribute to the destabilization of  
428 the atmosphere during the MJO. Since the associated wind bursts also accelerate the  
429 Yoshida-Wyrtki Jet, the contribution to the oceanic energy budget was sustained beyond  
430 the passage of the wind bursts. The Jet continued to decelerate from shear-induced  
431 turbulence at its base weeks after the passage of the wind bursts, and deep mixing from  
432 this turbulence limits the rate that SST increases in the subsequent suppressed MJO

433 phase. We note that recovery of SST following the relatively weak MJO1 (in terms of  
434 magnitude and rate-of-change of OLR and surface pressure, Figure 2d) was rapid and  
435 intense, followed by a relatively strong MJO2. After MJO2, SST recovery was slow and  
436 weak, followed by a relatively weak MJO3. An obvious issue that must be addressed is  
437 the potential role of this effect in retarding the formation and/or intensity of subsequent  
438 MJOs.

439

440 The upper ocean structure and processes of DYNAMO's hypothesis III were all observed  
441 in considerable detail during MJO2. The broader objective of assessing the roles of each  
442 of these in *controlling upper-ocean heat content and SST, and thereby surface flux*  
443 *feedback* to the atmosphere is now being actively pursued with these observations in  
444 hand. The results here suggest that tendencies of SST and turbulent surface heat fluxes  
445 change sign due to *wind- and shear-driven mixing, precipitation and their atmospheric*  
446 *cold pools, barrier layers, shallow diurnal warm layers and mixed layer entrainment*.

447

448 **ACKNOWLEDGEMENTS.** This work was funded through strongly cooperative  
449 interagency contributions from the Office of Naval Research, the National Science  
450 Foundation and the National Oceanic and Atmospheric Administration. We would  
451 like to acknowledge the significant leadership contributed by Prof. Chidong Zhang to the  
452 broader DYNAMO project.

453

454

**455 Sidebar 1 – Impact of Tropical Cyclone 05A on Sri Lanka**

456 As the first westerly wind burst (WWB1) of MJO2 propagated eastward over the ship at  
457 80.5°E, 0°N, a cyclonic vortex propagated westward 400-800 km to the north (Figure  
458 TC1). According to ECMWF deterministic analysis, the vortex was at 4°N and directly  
459 north of *Revelle* at 18:00 24 November, when the intense westerlies of the WWB1 near  
460 the equator and the westerly southern flank of the vortex coincided. This led to a  
461 significantly greater wind stress during WWB1 when the vortex was close to the ship,  
462 compared to that during WWB2.

463

464 On 25 November, southwesterly winds associated with the vortex caused severe weather  
465 at sea and important damage along the southern coast of Sri Lanka in Galle and Matara.  
466 Wind and intense rain in Galle and Matara were observed where the sheared core of the  
467 vortex intersected the southern coast of Sri Lanka on 06:00 26 November (Figure TC1c),  
468 followed by sustained onshore winds exceeding  $10 \text{ m s}^{-1}$  (Figure TC1d). The storm was  
469 responsible for casualties, including loss of 33 lives beginning 25 November, mostly  
470 fishermen at sea in small boats.

471

472 Though several numerical models predicted the formation of a large tropical disturbance  
473 south of Colombo, Sri Lanka, the fishermen had been provided no warning of the storm.  
474 A discussion of the local effects of the storm and potential repercussions can be followed  
475 in archives of the Sri Lankan newspaper *The Sunday Times*. The suffering of the people  
476 of Sri Lanka illustrates the significance of timely prediction and warnings of severe  
477 weather.

478

479 The tropical disturbance subsequently intensified to 25 knot ( $13 \text{ m s}^{-1}$ ) winds and was  
480 identified as tropical depression TC05A off the southern cape of India by the US Navy's  
481 Joint Typhoon Warning Center at 00:00 26 November. TC05A propagated  
482 northwestward into the Arabian Sea, reaching tropical storm status on 28 November, with  
483 maximum sustained winds of 35 kts ( $18 \text{ m s}^{-1}$ ).

484

**485 Sidebar 2 – Aerosol Response to the November MJO wind-burst**

486 Aerosols were sampled by a snorkel mounted above the bow deck (Figure 1—DeWitt et  
487 al., 2013; Bates et al., 2005). Size distributions and chemical compositions were  
488 measured on a nearly-continuous basis throughout the DYNAMO experiment. A  
489 schematic representation of the aerosol response to WWB1 reveals salient aspects of the  
490 aerosol evolution and suggests potential feedbacks between aerosol and convection in the  
491 remote Indian Ocean (Figure AE1).

492

493 Before the convective phase of MJO2 and its associated wind bursts (stage 1 in Figure  
494 AE1), low ozone levels and a buildup of sub- $\mu\text{m}$  aerosols prevailed. The aerosol was  
495 determined to be of either continental or marine origin by prevailing aerosol transport  
496 directions and chemical composition. Higher sub- $\mu\text{m}$  aerosol concentrations were  
497 measured from northerly, or continental, aerosol transport and lower for southerly, or  
498 clean marine, aerosol transport.

499

500 As convection intensified and became more frequent, air masses were injected from the  
501 upper atmosphere (stage 2), ozone levels rose and sub- $\mu\text{m}$  particles from aloft were  
502 introduced into the marine boundary layer. These sub- $\mu\text{m}$  aerosols, primarily comprised  
503 of sulfate, have the potential to act as cloud condensation nuclei (CCN; Kohler, 1936;  
504 Petters and Kreidenweis, 2007). The sharp increase in wind speed of WWB1 (stage 3)  
505 lofted super- $\mu\text{m}$  primary marine aerosol into the atmosphere while heavy rain  
506 simultaneously cleared the atmosphere of existing sub- $\mu\text{m}$  aerosol. This increased the  
507 aerosol surface area and thus the potential scattering surface, raising the aerosol optical

508 thickness, while reducing the total aerosol number and thus potential CCN concentrations  
509 (Figure AE1).

510

511 As demonstrated from these in situ aerosol measurements taken during the November  
512 MJO event, MJO-related convection had a significant effect on relative concentrations of  
513 sub- $\mu\text{m}$  continental and marine aerosol and super- $\mu\text{m}$  primary marine aerosol over the  
514 Indian Ocean (DeWitt et al., 2013). Changing aerosols translate into regional changes of  
515 the aerosol optical thicknesses and concentrations of available CCN in the remote Indian  
516 Ocean. Feedbacks to cloud formation, convective invigoration (Rosenfield et al., 2008),  
517 and the atmosphere's radiative budget are intriguing issues for future research.

518

**519 Sidebar 3 – Evolving cross-equatorial structure of the Yoshida-Wyrtki Jet**

520 Cross-equatorial transects of upper ocean currents measured using hull-mounted Doppler  
521 sonars were executed across 80.5°E on 03 October 2011, 10 November 2011 and 03  
522 December 2011 during passage to and from *Revelle*'s equatorial station (Figure XC1).  
523 These reveal the broad nature of the acceleration of zonal currents following the westerly  
524 wind bursts of MJO2 and hint at the deceleration processes thereafter.

525

526 The contrast between Figure XC1a and Figure XC1b is due almost completely to the  
527 wind-induced acceleration depicted in Figure 7. Zonal velocities increased throughout the  
528 4-degree longitude band straddling the equator, leading to a doubling of the volumetric  
529 transport in the eastward direction. The reason for the shallowing, weakening, and  
530 broadening of the westward-flowing undercurrent (Figure XC1c, ~180 – 300 m depth) is  
531 unclear but may represent a local thermocline response to the wind bursts. In this  
532 scenario, the greatly-increased current shear at the base of the eastward Yoshida-Wyrtki  
533 Jet contributes to stratified shear instability through reduction of the gradient Richardson  
534 number (proportional to the ratio of vertical gradients of density and velocity; Smyth et  
535 al, 2011). Resulting high turbulence levels carry eastward momentum down from the  
536 surface current and contribute to sea surface cooling for an extended period following the  
537 passage of MJO2.

538  
539

540 **REFERENCES**

- 541 Balaguru, K., P. Chang, R. Saravan, L/R. Leung, M. Liu and J-S. Hsieh, 2012: Ocean  
542 barrier layers' effect on tropical cyclone intensification. *Proc. Nat. Acad. Sci.*, **109**,  
543 14343-14347.
- 544
- 545 Bates, T. S., P. K. Quinn, D. J. Coffman, J. E. Johnson, and A. M. Middlebrook, 2005:  
546 Dominance of organic aerosols in the marine boundary layer over the Gulf of Maine  
547 during NEAQS 2002 and their role in aerosol light scattering, *J. Geophys. Res. Atmos.*,  
548 **110**, doi: 10.1029/2005JD005797.
- 549
- 550 Bell, T.L. and R. Suhasini, 1994: Principal modes of variation of rain-rate probability  
551 distribution. *J. Appl. Meteorol.*, **33**, 1067-1078.
- 552
- 553 Borge, J. C. N., K. Reichert, and J. Dittmer (1999): Use of nautical radar as a wave  
554 monitoring instrument, *Coastal Engineering*, **37**, 331–342.
- 555
- 556 Cifuentes-Lorenzen, A., J. B. Edson, C. J. Zappa, and L. Bariteau (2013): A multi-sensor  
557 comparison of ocean wave frequency spectra from a research vessel during the Southern  
558 Ocean Gas Exchange Experiment, *J. Atmos. Oceanic Tech.*, in revision.
- 559
- 560 Cronin, M.F. and M.J. McPhaden, 1997: The upper ocean heat balance in the western  
561 equatorial Pacific warm pool during September-December 1992. *J. Geophys. Res.*, **102**,  
562 8533-8553.

563

564 DeWitt, H.L., Coffman, D.J., Schulz, K.J., Brewer, W.A., Bates, T.S., Quinn, P.K., 2013:  
565 Atmospheric aerosol properties over the equatorial Indian Ocean and the impact of the  
566 Madden Julian Oscillation. *J. Geophys. Res. Atmos.*, **118**, 5736-5749.  
567 DOI:10.1002/jgrd.50419

568

569 Gottschalck, J., P.E. Roundy, C. J. Schreck III, A. Vintzileos, and C. Zhang, 2013: Large-  
570 scale atmospheric and oceanic conditions during the 2011-12 DYNAMO field campaign.  
571 *Mon. Weather Rev.*, accepted.

572

573 Johnson, R.H., and P.E. Ciesielski, 2013: Structure and properties of Madden-Julian  
574 Oscillations deduced from DYNAMO sounding arrays. *J. Atmos. Sci.* (in press)

575

576 Kiladis, G. N., M. C. Wheeler, P. T. Haertel, K. H. Straub, and P. E. Roundy, 2009:  
577 Convectively coupled equatorial waves, *Rev. Geophys.*, **47**, RG2003,  
578 doi:10.1029/2008RG000266.

579

580 Kohler, H., 1936: The nucleus in and the growth of hydroscopic droplets. *Trans Farad  
581 Soc.*, **32**, 1152-1161.

582

583 Madden, R. and P. Julian, 1971: Detection of a 40-50 day oscillation in the zonal wind in  
584 the tropical Pacific. *J. Atmos. Sci.*, **28**, 702-708.

585

- 586 Madden, R. and P. Julian, 1972: Description of global-scale circulation cells in the  
587 tropics with a 40-50 day period. *J. Atmos. Sci.*, **29**, 1109-1123.
- 588
- 589 McPhaden, M. J., G. Meyers, K. Ando, Y. Masumoto, V. S. N. Murty, M. Ravichandran,  
590 F. Syamsudin, J. Vialard, L. Yu, and W. Yu, 2009: RAMA - The Research Moored  
591 Array for African-Asian-Australian Monsoon Analysis and Prediction. *Bull. Amer.  
592 Meteor. Soc.*, **90**, 459-480.
- 593
- 594 Moreno G., L. Dagorn, G. Sancho and D. Itano, 2007: Fish behaviour from fishers'  
595 knowledge: the case study of tropical tuna around drifting fish aggregating devices  
596 (DFADs). *Can. J. Fish. Aquat. Sci.* **64**, 1517–1528.
- 597
- 598 Moum, J.N., M.C. Gregg, R-C. Lien and M.E. Carr, 1995: Comparison of turbulent  
599 kinetic energy dissipation rates from two ocean microstructure profilers, *J. Oceanic  
600 Atmos. Technol.*, **12**, 346–366.
- 601
- 602 Moum, J.N., R-C. Lien, A. Perlin, J.N. Nash, M.C. Gregg and P.J. Wiles, 2009: Sea  
603 surface cooling at the equator by subsurface mixing in tropical instability waves. *Nature  
604 Geoscience*, **2**, 761-765.
- 605
- 606 Petters, M.D. and S.M. Kreidenweis, 2007: A single particle representation of  
607 hygroscopic growth and cloud condensation nucleus activity. *Atmos Chem Phys.*, **7**,  
608 1961-1971.

- 609
- 610 Rosenfeld, D., U. Lohman, G. B. Raga, C. D. O'Dowd, M. Kulmala., S. Fuzzi,, A.
- 611 Reissell, M.N. Andreae, 2008: Flood or Drought: How Do Aerosols Affect Precipitation?
- 612 *Science*, **321**, 1309. DOI: 10.1126/science.1160606.
- 613
- 614 Roundy, P.E., 2008: Analysis of convectively-coupled Kelvin waves in the Indian Ocean
- 615 MJO. *J. Atmos. Sci.*, **65**, 1342-1359.
- 616
- 617 Rudich, Y., O. Khersonsky, D. Rosenfeld, 2002: Treating Clouds with a Grain of Salt.
- 618 *Geophys. Res. Lett.*, **29**, 10.1029/2002GL016055.
- 619
- 620 Schumacher, C., R.A. Houze and I. Kraucunas, 2004: The tropical dynamical response to
- 621 latent heating estimates derived from TRMM precipitation radar. *J. Atmos. Sci.*, **61**, 1341-
- 622 1358.
- 623
- 624 Short, D.A., P.A. Kucera, B.S. Ferrier, J.C. Gerlach, S.A. Rutledge and O.W. Thiele,
- 625 1997: Shipboard radar rainfall patterns within the TOGA COARE IFA. *Bull. Am. Met.*
- 626 *Soc.*, **78**, 2817-2836.
- 627
- 628 Smyth, W.D., J.N. Moum and J.D. Nash, 2011: Narrowband high-frequency oscillations
- 629 at the equator. Part II: Properties of shear instabilities. *J. Phys. Oceanogr.*, **41**, 412-428
- 630

- 631 Steiner, M., R.A. Houze and S.A. Yuter, 1995: Climatological characterization of three-  
632 dimensional storm structure from operational radar and rain gauge data. *J. Appl.*  
633 *Meteorol.*, **34**, 1978-2007.
- 634
- 635 Stephens, G. L., P. J. Webster, R. H. Johnson, R. Engelen, and T. S. L'Ecuyer, 2004:  
636 Observational evidence for the mutual regulation of the tropical hydrological cycle and  
637 tropical sea surface temperatures. *J. Climate*, **17**, 2213–2224.
- 638
- 639 Straub, K.H., and G.N. Kiladis, 2002: Observations of a convectively coupled Kelvin  
640 wave in the eastern Pacific ITCZ. *J. Atmos. Sci.*, **59**, 30-53.
- 641
- 642 Wyatt, L. R., J. J. Green, K.-W. Gurgel, J. C. N. Borge, K. Reichert, K. Hessner, H.  
643 Günther, W. Rosenthal, O. Saetra, and M. Reistad (2003), Validation and  
644 intercomparisons of wave measurements and models during the EuroROSE experiments,  
645 *Coastal Engineering*, **48**, 1–28.
- 646
- 647 Wyrtki, K., 1973: An equatorial jet in the Indian Ocean. *Science*, **181**, 262-264.
- 648
- 649 Yoneyama, K., C. Zhang and C.N. Long, 2013: Tracking pulses of the Madden-Julian  
650 Oscillation. *Bull.Amer.Meteor.Soc.*, accepted.
- 651
- 652 Yoshida, K. 1959: A theory of the Cromwell Current (the Equatorial Undercurrent) and  
653 of the equatorial upwelling—An interpretation in a similarity to a coastal circulation. *J.*

- 654      *Oceanogr. Soc. Jpn.*, **15**, 159–170.
- 655
- 656      Yuter, S.A. and R.A. Houze, 1998: The natural variability of precipitating clouds over the  
657      western Pacific warm pool. *Q. J. Roy. Met. Soc.*, **124**, 53-99.
- 658
- 659      Zhang, C., 2005: Madden-Julian Oscillation. *Rev. Geophys.*, **43**, RG2003,  
660      doi:10.1029/2004RG000158.
- 661
- 662      Zhang, C., 2013: Madden-Julian Oscillation: Bridging Weather and Climate. Bull.  
663      Amer. Met. Soc., accepted.
- 664
- 665

666   **List of Tables**

667

668   **Table 1** – Measurements referred to in text, with responsible parties.

669

670

671   **List of Figures**

672

673   **Figure 1**- Measurement systems installed on *R/V Roger Revelle* for DYNAMO. Inset  
674   map shows locations of land-based sounding stations, oceanographic moorings and the  
675   research vessels *Mirai* and *Revelle* during the intensive observation period of DYNAMO.  
676   The black line outlines the flight track of the NOAA P3 research aircraft on 24 November  
677   2011.

678   **Figure 2** - Time series at 0°, 80.5°E during DYNAMO. a) Outgoing longwave radiation  
679   (OLR; shaded) from the Advanced Very High Resolution Radiometer (AVHRR)  
680   instrument aboard the NOAA polar orbiting spacecraft, and surface pressure (blue line)  
681   from the nearby RAMA surface meteorological buoy. b) Zonal wind speed. Ship (10  
682   minute averages, thin lines) and RAMA (daily averages; thick lines) measurements are  
683   shown for all series where available. c) Zonal current speed at 20 m depth. d) SST  
684   (black), temperatures at 1 m (thick blue) and 5 m (thin blue). e) Air temperatures from  
685   *Revelle* and RAMA with SST repeated for direct comparison. f) Surface heat fluxes  
686   partitioned into incoming solar radiation, outgoing longwave radiation, sensible heat and  
687   latent heat. The fluxes are defined as positive down; values > 0 represent heating of the  
688   ocean by the atmosphere.

689   **Figure 3** - a) Hovmoller plot of TRMM precipitation at the equator and across the Indian  
690   Ocean for the period of MJO2 (blue image color); corresponding contours of OLR = 200  
691   W m<sup>-2</sup> (black). Green lines indicate propagating disturbances in TRMM at roughly the

atmospheric Kelvin wave speed,  $8.6 \text{ m s}^{-1}$ . Note that the OLR signal travels more slowly than the rain signal. b) Time series of precipitation - from TRMM (blue shading; averaged  $\pm 0.5^\circ$  about the equator) and from shipboard C-band radar (black; convective and stratiform components are shown in off-greens). Standard convective and stratiform echo partitioning methods (Steiner et al., 1995; Yuter and Houze, 1998) were used with a 35 dBz threshold. Separate Z-R relationships derived from Gan and Manus Island 2DVD data during DYNAMO were employed to calculate areal average radar rain rate for each precipitation type. These relationships are  $Z_{\text{CONV}} = 61.118 R^{1.58}$  and  $Z_{\text{STRAT}} = 200.47 R^{1.511}$  (linear reflectivity units and mm hr $^{-1}$  rainfall units). All calculations were performed at 1 km height on gridded radar data (2 km horizontal, 0.5 km vertical resolution), out to 100 km range. c) Time series of ship-measured wind stress (black shading).

**Figure 4** - a) Potential temperature anomaly. b) Specific humidity anomaly. c) Zonal wind in the troposphere above the ship *Revelle* from rawinsondes. d) Temperatures values at 10-m height and the sea surface. e) Specific humidity values at 10-m and the sea surface. The vertical coordinate is mass-weighted in (a) – (c). Grey vertical lines indicate missing data. The 400-hPa vertical velocity computed from the northern array soundings (Johnson and Ciesielski, 2013) is shown in (a, right axis). Two-day running averages are plotted in (d) - (e) to provide the overall trends.

**Figure 5** - Time series of wind and waves at *Revelle* showing the arrival of the first wind burst of MJO2. a) Wind stress (black) and significant wave height (blue) as measured from motion-corrected laser altimeter. b) Spectrogram of wave height. c) Averaged

714 spectra (in variance-preserving form) representing periods 6 h prior to the arrival of the  
715 wind burst (03:00-09:00) and 6 h following (13:00-19:00).

716 **Figure 6** - Structure of the near surface of the ocean as the leading wind burst of MJO2  
717 arrived at *Revelle*. a) Net surface heat flux. b) Surface wind stress. c) Ocean temperature  
718 at 2.0, 3.9 and 7.1 m (depths denoted by white dots in d). d) Image-color plot of  
719 temperature in the upper 8 m from sensors at depths indicated at left and sampling as they  
720 are profiling the water column with wave motion.

721 **Figure 7** - Summary time series of upper ocean response to the first westerly wind burst  
722 of MJO2 at *Revelle* on 24 November 2011. a) The wind stress (total) appears as a step  
723 function change from  $<0.05 \text{ N m}^{-2}$  to  $>0.5 \text{ N m}^{-2}$  in a few minutes. b) Net surface heating.  
724 Net surface cooling lasted for more than 1 day, a rarity at the equator, though common  
725 during the passage of MJO events. c) Zonal current. The eastward surface current (the  
726 Yoshida-Wyrtki Jet) accelerated from  $< 0.5 \text{ m s}^{-1}$  in about 1 day, deepening with time.  
727 The mixed layer is indicated by the black line, the potential density surface 1024.75 by  
728 the white line. d) Temperature. Mixed layer cooling was driven by combined atmospheric  
729 and subsurface cooling. e) Salinity. Salinification of the surface was driven by an excess  
730 of subsurface mixing over precipitation. f) Turbulence dissipation. At bottom are  
731 expanded plots showing the first 24 h following arrival of the wind burst. g) Wind stress.  
732 h) Temperature with temperature contours scaled to represent identical contribution to  
733 density as do salinity contours in i) salinity.

734  
735 **Figure TC1** - Surface wind vectors and speed (shaded) every 12 hours (ECMWF  
736 deterministic analysis) illustrate eastward propagation of WWB1 across 80°E and

737 centered on the equator coincident with westward propagation and intensification of a  
738 cyclonic vortex north of the equator across that longitude.

739

740 **Figure AE1-** a) Schematic of aerosol response separated into three observed temporal  
741 stages of MJO passage at 0°, 80°E. b) Log-normalized surface area size distribution  
742 ( $dSdlogD_p$ ) of aerosols from 0.02-10  $\mu\text{m}$ . c) Number concentration of aerosols as a  
743 function of aerosol diameter. Color scales are shown at bottom. Overlaid on b,c) is ozone  
744 concentration in parts per billion by volume (ppbv) in black.

745  
746 **Figure XC1** – Cross-equatorial structure of zonal currents at 80°E from 2°S (left) to 2°N  
747 a) before and b) following the westerly wind burst during MJO2. Eastward transports  
748 represent the volumetric flow rate through the cross-section above 100 m in units of  
749 Sverdrups (1 Sv =  $10^6 \text{ m}^3 \text{ s}^{-1}$ ). c) Average velocity profiles between 1°S and 1°N on 03  
750 October, 10 November and 03 December. d) Corresponding average profiles of zonal  
751 current shear,  $du/dz$ .

752

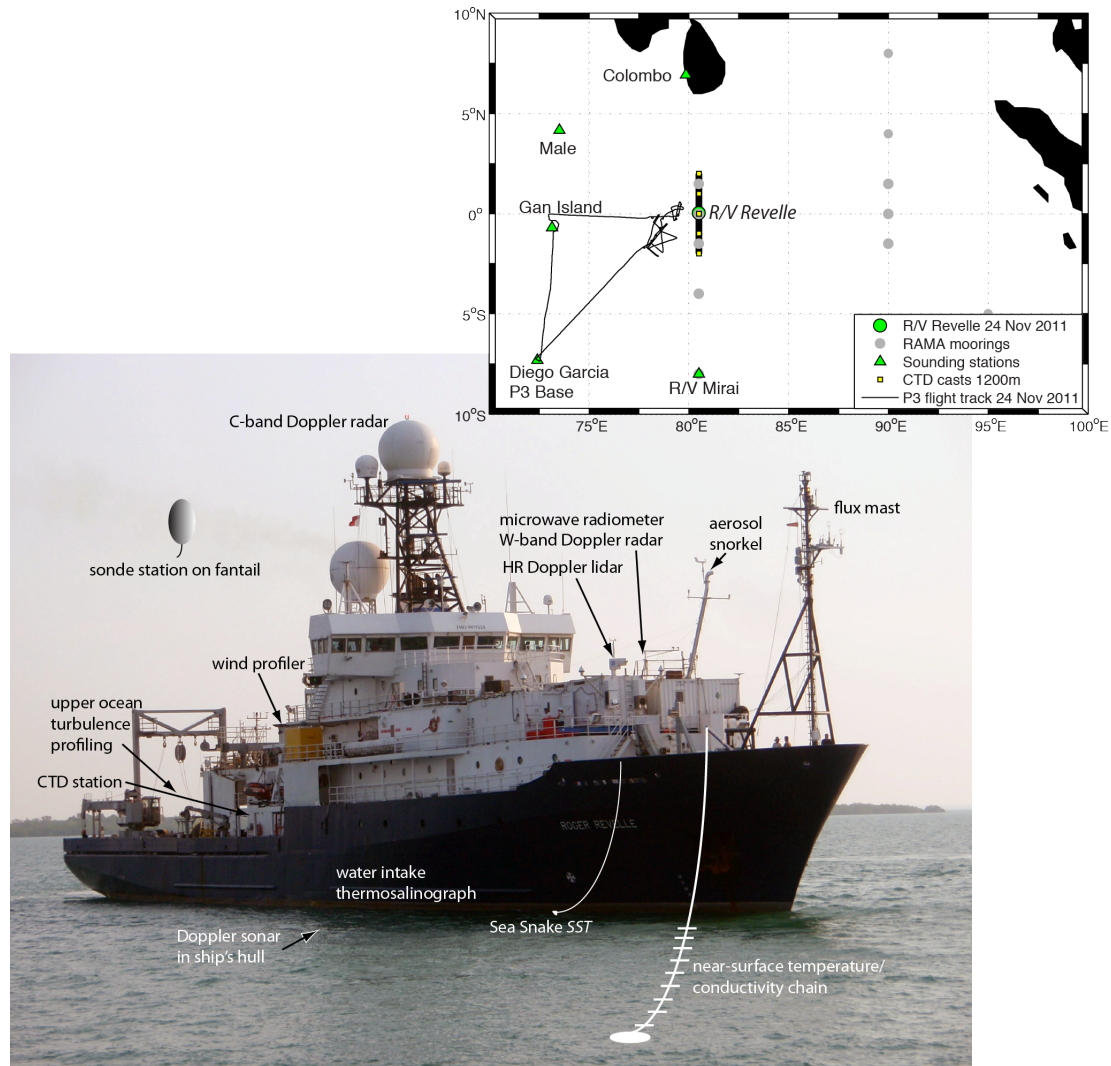
753

Instruments	Institution	Team Leader	PI
<b>Radiosondes</b>	NCAR/CSU	Bill Brown	Richard Johnson
<b>Wind profiler</b>		NCAR	Colorado State U.
<b>Flux mast</b>	NOAA ESRL	Dan Wolfe, Ludovic	Simon DeSzeoke
<b>W-band Doppler</b>	Physical Science Division	Bariteau	(Oregon State U.)
<b>Microwave radiometer</b>		NOAA ESRL	James Edson (U. Connecticut)
<b>Sea snake</b>			Chris Fairall (NOAA ESRL)
<b>Longwave Radiometers</b>	LDEO of Columbia University		Christopher Zappa (LDEO)
<b>High-Resolution Doppler lidar</b>	NOAA ESRL Physical Science Division	Alan Brewer NOAA ESRL	Alan Brewer NOAA ESRL
<b>C-band Doppler radar</b>	Colorado State U.	John Gerlach NASA GSFC	Steven Rutledge Colorado State U.
<b>Aerosol chemistry</b>	NOAA PMEL atmospheric chemistry group	Derek Coffman, Langley DeWitt NOAA/PMEL	Timothy Bates NOAA/PMEL
<b>Upper ocean measurements</b>	Oregon State U. Ocean Mixing group	James Moum Oregon State U.	James Moum Oregon State U.

754

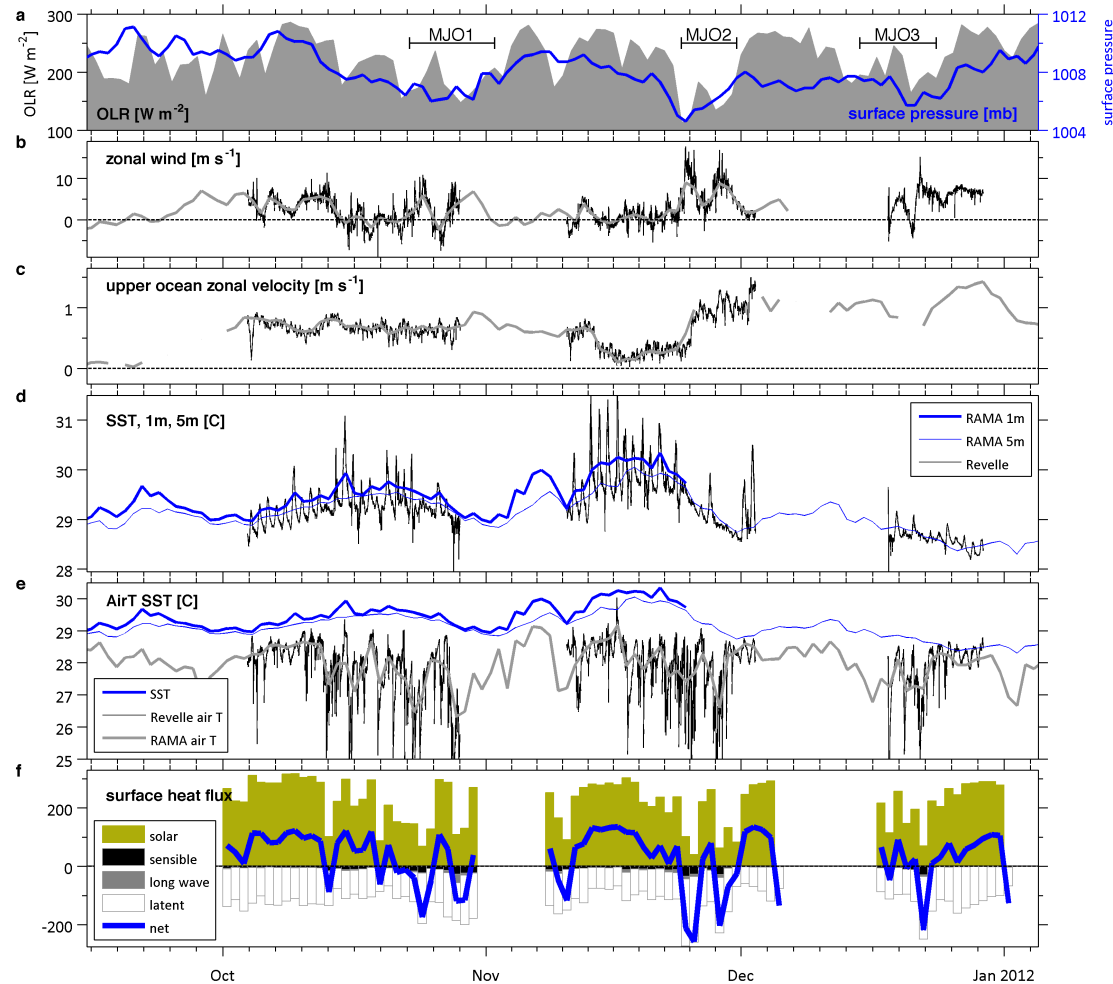
755

Table 1 – List of measurements referred to in text, with responsible parties.



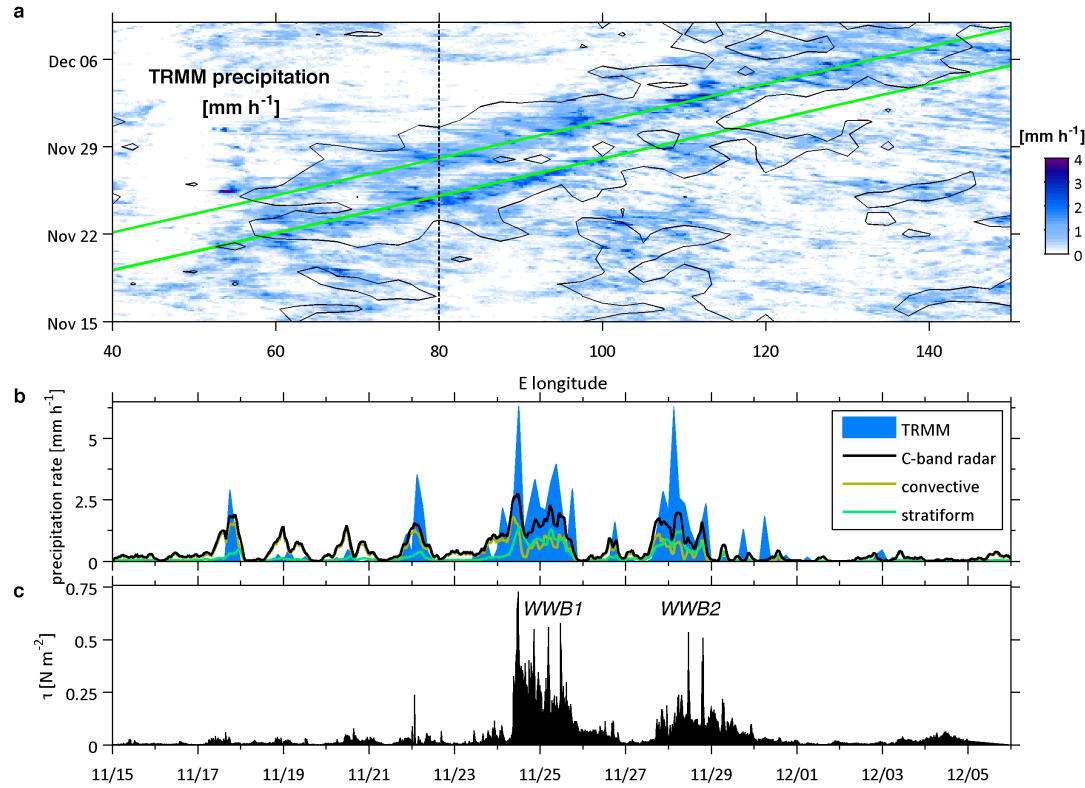
756

757 **Figure 1-** Measurement systems installed on *R/V Roger Revelle* for DYNAMO. Inset  
 758 map shows locations of land-based sounding stations, oceanographic moorings and the  
 759 research vessels *Mirai* and *Revelle* during the intensive observation period of DYNAMO.  
 760 The black line outlines the flight track of the NOAA P3 research aircraft on 24 November  
 761 2011.



762

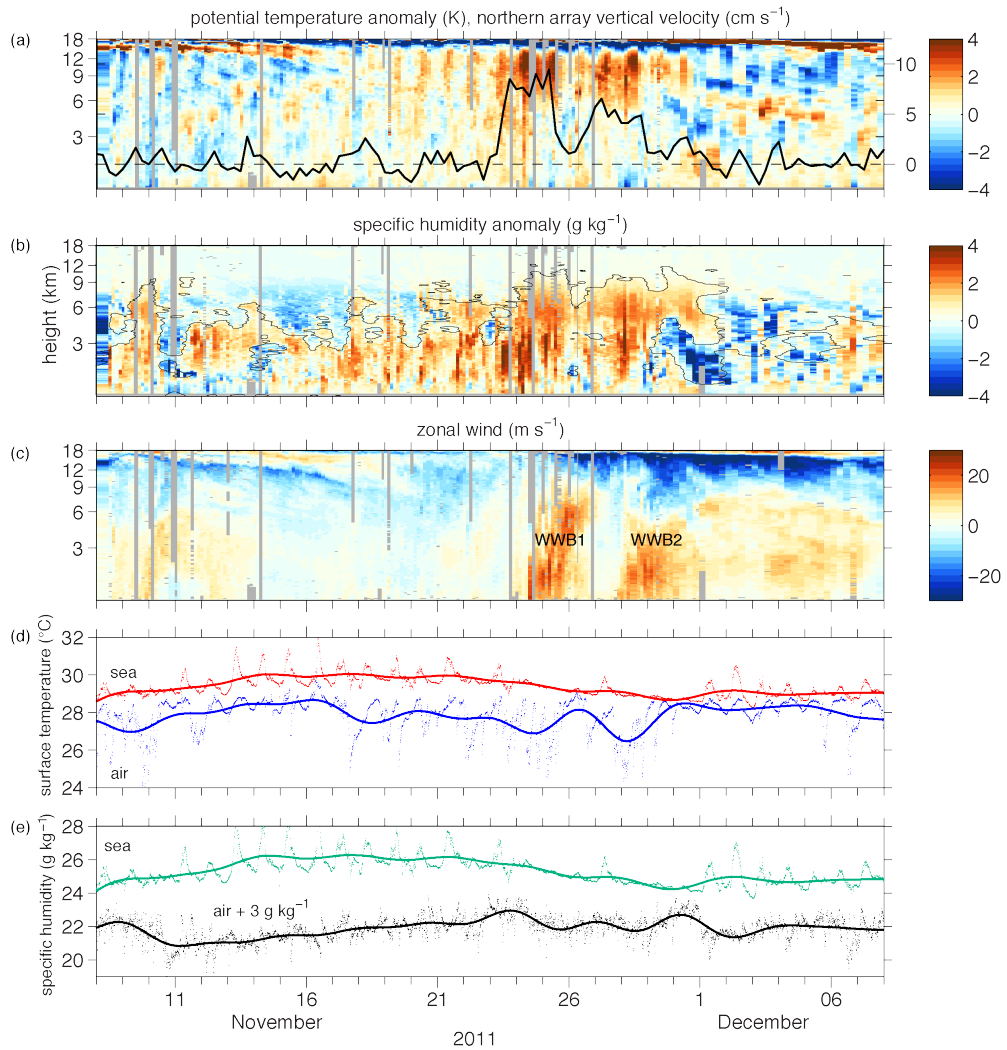
763 **Figure 2** - Time series at 0°, 80.5°E during DYNAMO. a) Outgoing longwave radiation  
 764 (OLR; shaded) from the Advanced Very High Resolution Radiometer (AVHRR)  
 765 instrument aboard the NOAA polar orbiting spacecraft, and surface pressure (blue line)  
 766 from the nearby RAMA surface meteorological buoy. b) Zonal wind speed. Ship (10  
 767 minute averages, thin lines) and RAMA (daily averages; thick lines) measurements are  
 768 shown for all series where available. c) Zonal current speed at 20 m depth. d) SST  
 769 (black), temperatures at 1 m (thick blue) and 5 m (thin blue). e) Air temperatures from  
 770 *Revelle* and RAMA with SST repeated for direct comparison. f) Surface heat fluxes  
 771 partitioned into incoming solar radiation, outgoing longwave radiation, sensible heat and  
 772 latent heat. The fluxes are defined as positive down; values > 0 represent heating of the  
 773 ocean by the atmosphere.



774

775 **Figure 3 - a)** Hovmöller plot of TRMM precipitation at the equator and across the Indian  
 776 Ocean for the period of MJO2 (blue image color); corresponding contours of OLR = 200  
 777 W m<sup>-2</sup> (black). Green lines indicate propagating disturbances in TRMM at roughly the  
 778 atmospheric Kelvin wave speed, 8.6 m s<sup>-1</sup>. Note that the OLR signal travels more slowly  
 779 than the rain signal. b) Time series of precipitation - from TRMM (blue shading;  
 780 averaged  $\pm 0.5^\circ$  about the equator) and from shipboard C-band radar (black; convective  
 781 and stratiform components are shown in off-greens). Standard convective and stratiform  
 782 echo partitioning methods (Steiner et al., 1995; Yuter and Houze, 1998) were used with a  
 783 35 dBz threshold. Separate Z-R relationships derived from Gan and Manus Island 2DVD  
 784 data during DYNAMO were employed to calculate areal average radar rain rate for each  
 785 precipitation type. These relationships are  $Z_{\text{CONV}} = 61.118 R^{1.58}$  and  $Z_{\text{STRAT}} = 200.47$   
 786  $R^{1.511}$  (linear reflectivity units and mm hr<sup>-1</sup> rainfall units). All calculations were  
 787 performed at 1 km height on gridded radar data (2 km horizontal, 0.5 km vertical  
 788 resolution), out to 100 km range. c) Time series of ship-measured wind stress (black  
 789 shading).

790



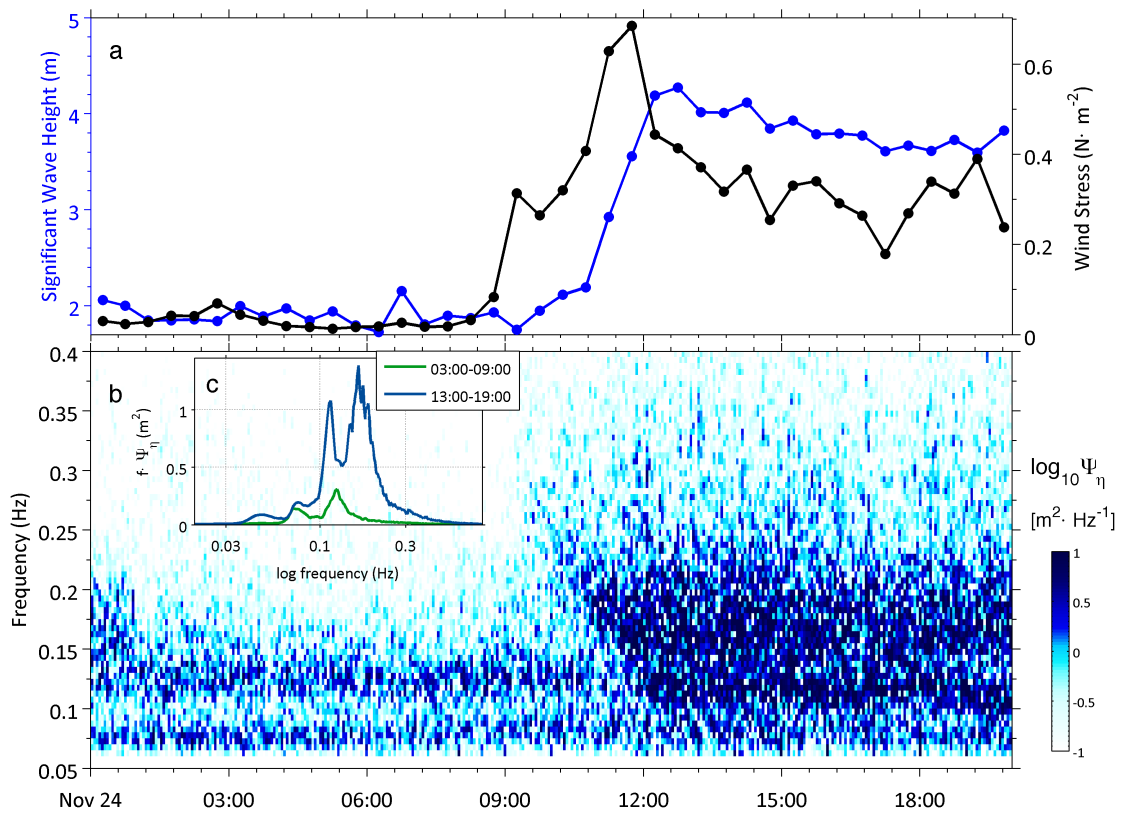
791  
792  
793  
794  
795  
796  
797  
798

**Figure 4 -** a) Potential temperature anomaly. b) Specific humidity anomaly. c) Zonal wind in the troposphere above the ship *Revelle* from rawinsondes. d) Temperatures values at 10-m height and the sea surface. e) Specific humidity values at 10-m and the sea surface. The vertical coordinate is mass-weighted in (a) – (c). Grey vertical lines indicate missing data. The 400-hPa vertical velocity computed from the northern array soundings (Johnson and Ciesielski, 2013) is shown in (a, right axis). Two-day running averages are plotted in (d) - (e) to provide the overall trends.

799

800

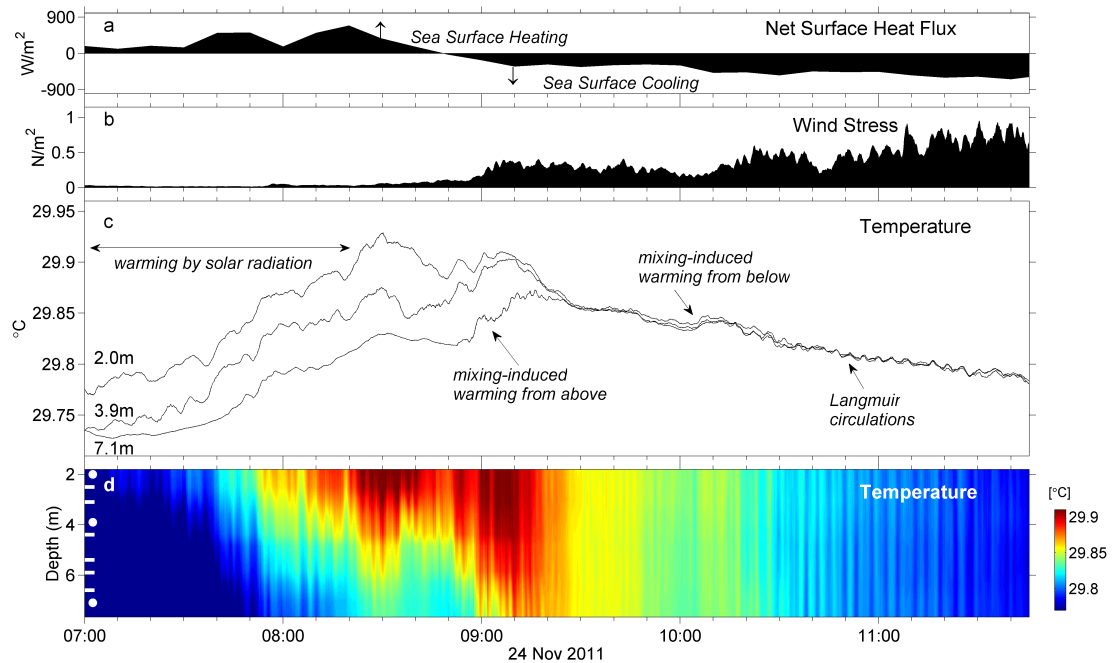
801



802

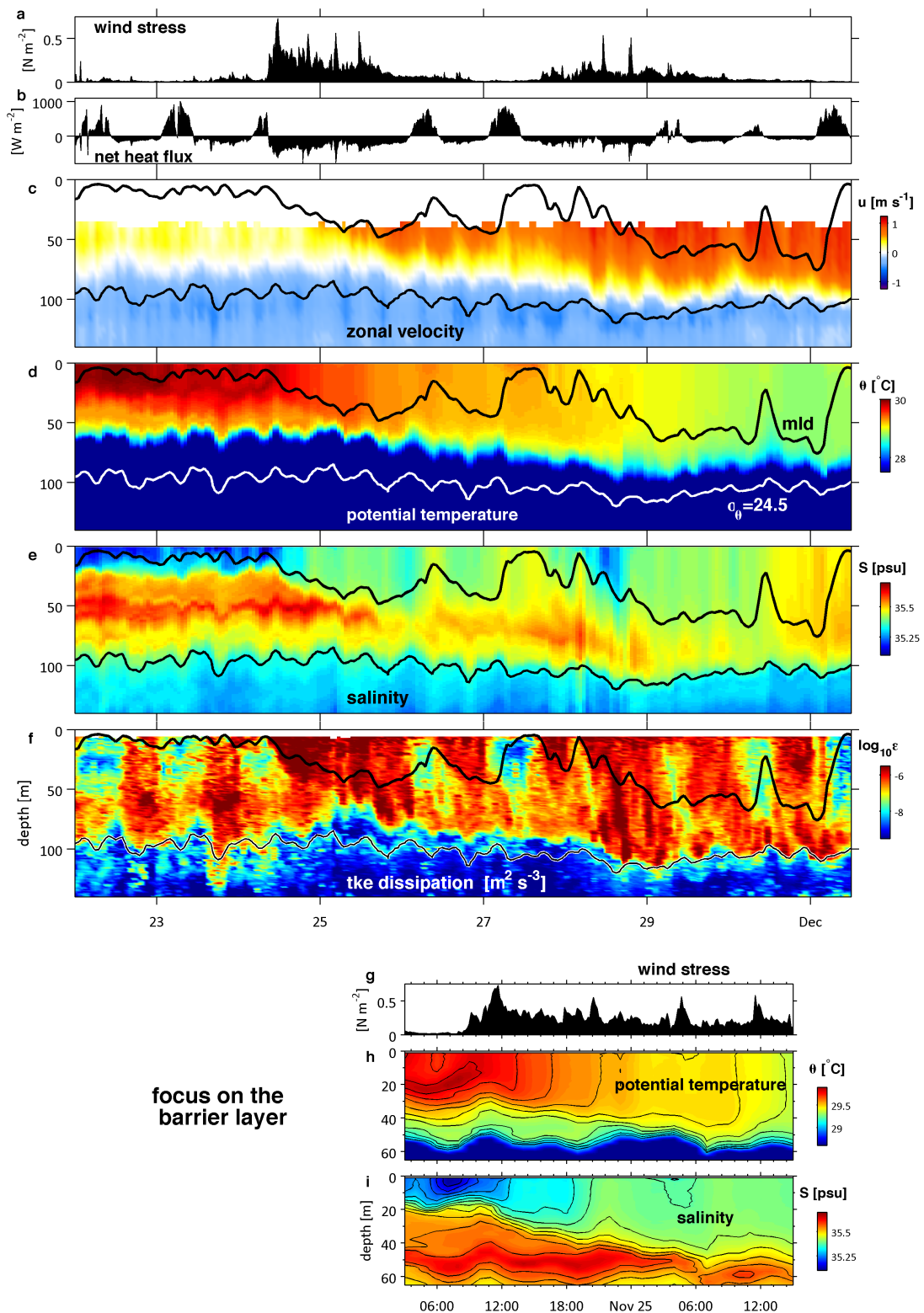
803 **Figure 5** - Time series of wind and waves at *Revelle* showing the arrival of the first wind  
 804 burst of MJO2. a) Wind stress (black) and significant wave height (blue) as measured  
 805 from motion-corrected laser altimeter. b) Spectrogram of wave height. c) Averaged  
 806 spectra (in variance-preserving form) representing periods 6 h prior to the arrival of the  
 807 wind burst (03:00-09:00) and 6 h following (13:00-19:00).

808



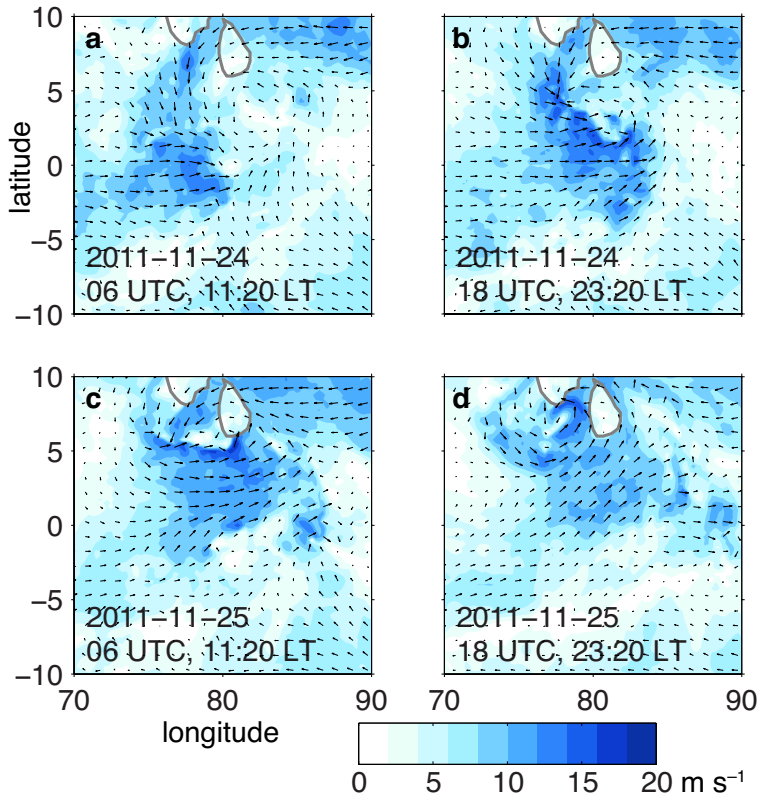
809

810      **Figure 6** - Structure of the near surface of the ocean as the leading wind burst of MJO2  
 811      arrived at *Revelle*. a) Net surface heat flux. b) Surface wind stress. c) Ocean temperature  
 812      at 2.0, 3.9 and 7.1 m (depths denoted by white dots in d). d) Image-color plot of  
 813      temperature in the upper 8 m from sensors at depths indicated at left and sampling as they  
 814      are profiling the water column with wave motion.



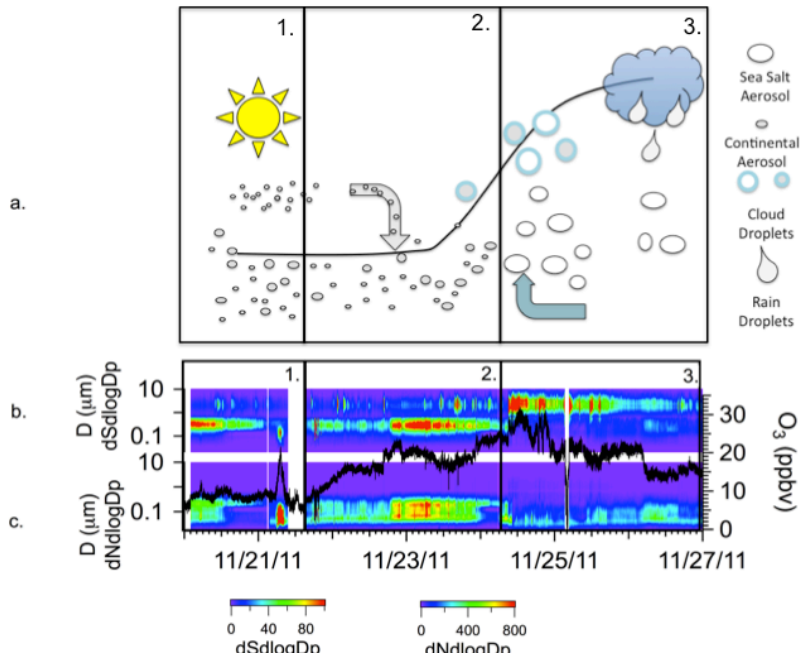
816 **Figure 7** - Summary time series of upper ocean response to the first westerly wind burst  
817 of MJO2 at *Revelle* on 24 November 2011. a) The wind stress (total) appears as a step  
818 function change from  $<0.05 \text{ N m}^{-2}$  to  $>0.5 \text{ N m}^{-2}$  in a few minutes. b) Net surface heating.  
819 Net surface cooling lasted for more than 1 day, a rarity at the equator, though common  
820 during the passage of MJO events. c) Zonal current. The eastward surface current (the  
821 Yoshida-Wyrtki Jet) accelerated from  $< 0.5 \text{ m s}^{-1}$  in about 1 day, deepening with time.  
822 The mixed layer is indicated by the black line, the potential density surface 1024.75 by  
823 the white line. d) Temperature. Mixed layer cooling was driven by combined atmospheric  
824 and subsurface cooling. e) Salinity. Salinification of the surface was driven by an excess  
825 of subsurface mixing over precipitation. f) Turbulence dissipation. At bottom are  
826 expanded plots showing the first 24 h following arrival of the wind burst. g) Wind stress.  
827 h) Temperature with temperature contours scaled to represent identical contribution to  
828 density as do salinity contours in i) salinity.

829



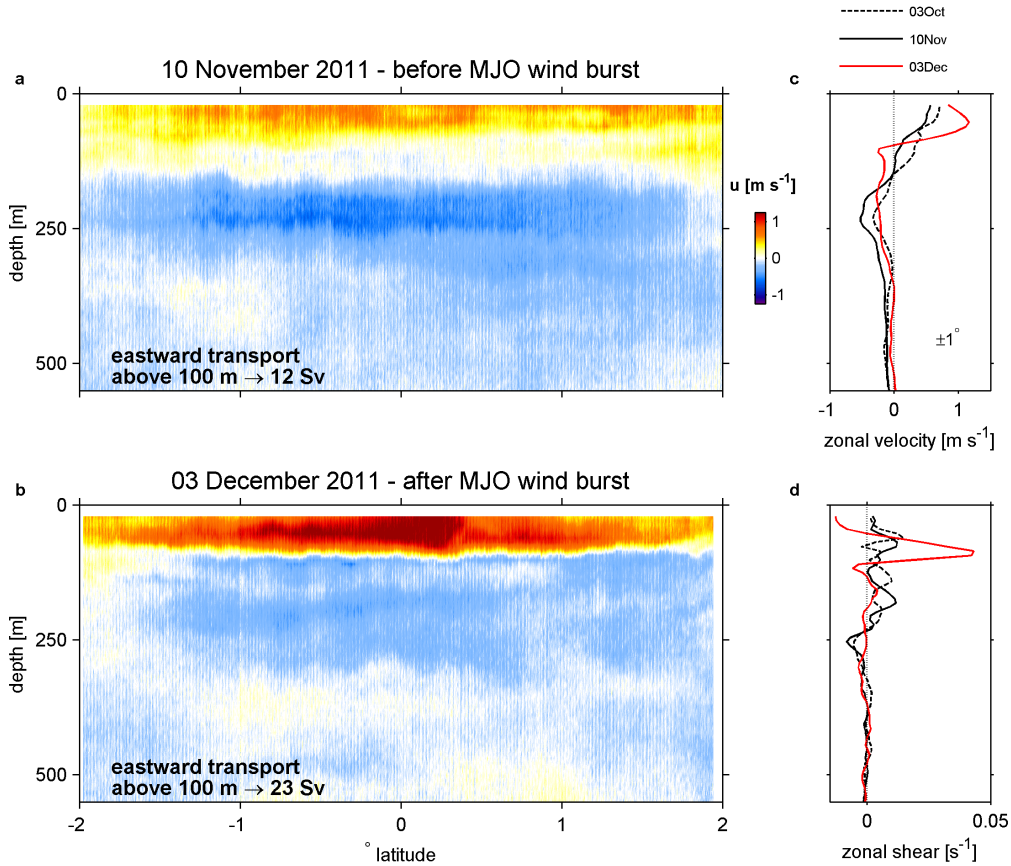
830

831 **Figure TC1** - Surface wind vectors and speed (shaded) every 12 hours (ECMWF  
832 deterministic analysis) illustrate eastward propagation of WWB1 across 80°E and  
833 centered on the equator coincident with westward propagation and intensification of a  
834 cyclonic vortex north of the equator across that longitude.



835  
 836 **Figure AE1-** a) Schematic of aerosol response separated into three observed temporal  
 837 stages of MJO passage at  $0^\circ$ ,  $80^\circ\text{E}$ . b) Log-normalized surface area size distribution  
 838 ( $dSd\log D_p$ ) of aerosols from  $0.02$ - $10 \mu\text{m}$ . c) Number concentration of aerosols as a  
 839 function of aerosol diameter. Color scales are shown at bottom. Overlaid on b,c) is ozone  
 840 concentration in parts per billion by volume (ppbv) in black.

841



842

843 **Figure XC1** – Cross-equatorial structure of zonal currents at 80°E from 2°S (left) to 2°N  
 844 a) before and b) following the westerly wind burst during MJO2. Eastward transports  
 845 represent the volumetric flow rate through the cross-section above 100 m in units of  
 846 Sverdrups ( $1 \text{ Sv} = 10^6 \text{ m}^3 \text{s}^{-1}$ ). c) Average velocity profiles between 1°S and 1°N on 03  
 847 October, 10 November and 03 December. d) Corresponding average profiles of zonal  
 848 current shear,  $du/dz$ .